Reports

Electrodeposited Ceramic Superlattices

JAY A. SWITZER,* MICHAEL J. SHANE, RICHARD J. PHILLIPS

Ceramic superlattices have been produced by electrodeposition with modulation wavelengths in the range from 5 to 10 nanometers. The $Tl_aPb_bO_c$/$Tl_dPb_eO_f$ superlattices were deposited from a single aqueous solution at room temperature, and the layer thicknesses were galvanostatically controlled. The films showed strong preferred orientation and distinct first-order satellites around the Bragg reflections in the x-ray diffraction pattern. The modulation wavelengths calculated from the satellite spacings were in agreement with those calculated from Faraday's law. Because the modulation wavelengths are of electron mean free path dimensions, this class of degenerate semiconductor metal-oxide superlattices may exhibit thickness-dependent quantum optical, electronic, or optoelectronic effects.

CERAMICS ARE GENERALLY VIEWED as highly insulating refractory materials with coarse microstructures. They are both processed and used at high temperatures. We report the room-temperature electrochemical deposition of nanomodulated (nanometer-scale modulation wavelengths) ceramic superlattice thin films. An idealized superlattice structure is shown in Fig. 1. The material is abruptly modulated with respect to composition or structure, or both. When the modulation wavelength, Λ, is in the nanometer range, each layer is only a few unit cells thick.

Although superlattice structures have been fabricated with metallic (*1*), semiconductor (*2*), and ceramic (*3*) materials, the major device emphasis has been on semiconductor-based systems (*2, 4*). Semiconductor superlattice devices are usually multiple quantum well structures, in which nanometer-scale layers of a lower bandgap material such as GaAs are sandwiched between layers of a larger bandgap material such as GaAlAs. Quantum effects, such as enhanced carrier mobility (two-dimensional electron gas) and bound states in the optical adsorption spectrum, and nonlinear optical effects, such as intensity-dependent refractive indices, have been observed in nanomodulated semiconductor multiple quantum wells. Examples of devices based on these structures include fast optical switches, high electron mobility transistors, and quantum well lasers.

Our emphasis is on nanomodulated ceramic superlattices that are based on materials with bandgaps in the 1.5- to 3.0-eV range. These structures may also show quantum electronic, optical, or optoelectronic effects as the modulation wavelength approaches the electron mean free path. We are interested in oxide superlattices in which the bandgap, carrier type, and carrier concentration can, in principle, be periodically varied over a larger range than is possible with semiconductor or metallic superlattices.

The focus of our initial work in this area has been on the electrochemical atomic-level architecture of compositionally modulated thin films made from metal-oxide degenerate semiconductors. We have chosen the $Tl_aPb_bO_c$/$Tl_dPb_eO_f$ system because of our earlier experience with the electrochemical and photoelectrochemical deposition of highly oriented films of thallium(III) oxide (*5–8*). Also, the room-temperature electrodeposition of PbO_2 (*9–11*) and $Pb_8Tl_5O_{24}$ (*12, 13*) are well documented.

Several workers have shown that compositionally modulated metallic alloys can be electrochemically deposited if either the potential or the current is cycled in a single plating solution containing salts or complexes of both metals (*14–21*). Recently, Lashmore and Dariel (*19*) and Yahalom *et al.* (*20*) have deposited metallic superlattices with nanometer-scale modulation wavelengths. The interest in nanomodulated metallic systems stems from their enhanced mechanical and magnetic properties (*1, 16, 22–24*).

The electrochemical method offers several advantages over vapor deposition methods such as molecular beam epitaxy for depositing nanomodulated materials with nearly square-wave modulation of composition and structure, because the low processing temperatures minimize interdiffusion. In addition, one can control the film thickness by monitoring the delivered charge, films can be deposited onto complex shapes, and the technique is not capital intensive.

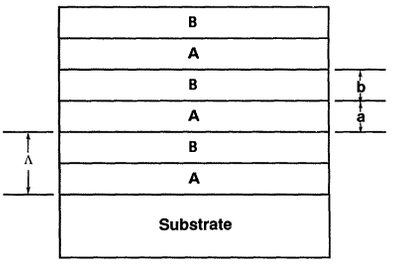

Fig. 1. Idealized superlattice structure with square-wave modulation of composition or structure, or both. The thicknesses a and b are not necessarily equal, as long as the structure is periodic.

We assume that three criteria must be satisfied in order to electrodeposit a nanomodulated ceramic film as represented in Fig. 1: (i) the materials should deposit directly as anhydrous oxides, (ii) the composition of the films should be dependent on the applied potential or current, and (iii) the layers A and B should be nearly isomorphous. If lattice mismatch is too great, the materials will not grow epitaxially.

The $Tl_aPb_bO_c$/$Tl_dPb_eO_f$ system appears to satisfy all of these criteria. The deposition potentials for the end members, Tl_2O_3 and PbO_2, differ by only 0.26 V, so there is considerable overlap of the electrodeposition current-voltage (*iV*) curves. One can systematically vary the Pb/Tl ratio in the electrodeposited oxide films by changing the applied anodic current (Table 1). The Pb/Tl ratio was varied from 0.84 at 0.05 mA to 7.3 at 5.0 mA.

The questions of crystal structure and lattice mismatch are not so easily answered. Surprisingly, the mixed metal oxides deposited at these different currents have very similar cubic structures. This is unexpected,

Table 1. Composition and values of the cubic lattice parameters for electrodeposited oxide films as a function of applied current. The solution was 0.005*M* $TlNO_3$ and 0.1*M* $Pb(NO_3)_2$, in 5*M* NaOH, and the electrode was polycrystalline 430 stainless steel. The Pb/Tl ratio was determined by energy-dispersive x-ray analysis in the scanning electron microscope. SCE is the standard calomel reference electrode.

Applied current (mA)	Measured potential (V versus SCE)	Pb/Tl mole ratio	Cubic lattice parameter (nm)
0.05	0.06	0.84	0.536
0.5	0.12	1.9	0.535
1.0	0.14	2.5	0.537
5.0	0.27	7.3	0.535

Department of Materials Science and Engineering, University of Pittsburgh, Pittsburgh, PA 15261.

*To whom correspondence should be addressed.

Table 2. Comparison of modulation wavelengths calculated from Faraday's law (Λ_F) and from x-ray satellite spacing (Λ_x) for ceramic superlattices deposited at various currents and dwell times. We calculated Λ_F from Eq. 1, assuming ρ = 10.353 g/cm^3, n = 2, and M = 228 g/mol. We calculated Λ_x from Eq. 2, using positions of satellites around Bragg reflections in the x-ray diffraction pattern (λ = 0.15418 nm).

i_a (mA)	t_a (s)	i_b (mA)	t_b (s)	Area A (cm^2)	Λ_F (nm)	Λ_x (nm)
5.0	0.4	0.05	40	0.78	5.9	5.9
5.0	0.5	0.05	50	0.78	7.3	7.3
5.0	0.6	0.05	60	0.83	8.3	8.5
1.0	2.0	0.05	40	0.79	5.8	5.8
1.0	3.0	0.05	60	0.80	8.6	8.4

because the metal ions have different valences and ionic radii. In addition, Tl_2O_3 (*25*) has the body-centered cubic bixbyite structure (a = 1.05434 nm), whereas PbO_2 (*26*) is either orthorhombic (α-PbO_2) or tetragonal (β-PbO_2). Values of the cubic lattice parameters for the electrodeposited mixed oxides are listed in Table 1. Substitution of Tl_2O_3 into PbO_2 appears to stabilize a face-centered cubic (fcc) structure with an average lattice parameter a of 0.536 nm. This agrees with the results of work by Sakai *et al.*, in which they electrodeposited an oxide with nominal composition $Pb_8Tl_5O_{24}$, which had an fcc structure, with a = 0.53331 nm (*12*). There is also evidence for a cubic polymorph of PbO_2 (a = 0.53492 nm), which exists at high pressures (*27*). The values of a that we measured for our mixed oxides vary by only 0.3% over the entire composition range listed in Table 1.

We deposited modulated films by applying a square-wave galvanostatic pulse. A generalized waveform is shown in Fig. 2. Oxide A with a high Pb/Tl ratio is deposited at high current i_a with short dwell time t_a, and oxide B with a lower Pb/Tl ratio is deposited at low current i_b with long dwell time t_b. The modulation wavelength, Λ_F, can be estimated from Eq. 1, which is derived from Faraday's law:

$$\Lambda_F = \frac{1}{nFA}\left(\frac{i_a\, t_a\, M_a}{\rho_a} + \frac{i_b\, t_b\, M_b}{\rho_b}\right) \quad (1)$$

where n is the number of electrons transferred, F is Faraday's number, A is the electrode area, M is the formula weight, and ρ is the density. We estimate that 1.1 to 1.2 μm of material are deposited per coulomb per centimeter squared.

We electrodeposited one of the superlattice structures onto a polycrystalline 430 stainless steel substrate by alternately pulsing at 5 mA for 0.5 s and 0.05 mA for 50 s in a solution of 0.005M $TlNO_3$ and 0.1M $Pb(NO_3)_2$ in 5M NaOH. The x-ray diffraction pattern for the material is shown in Fig. 3. Two intense Bragg peaks are observed at 2θ values (θ is the dispersion angle) of approximately 34° and 71°, which can be indexed as (200) and (400) reflections (*12*). The high intensities of these reflections relative to others in the pattern is a good indication of strong preferred orientation, with cube faces growing parallel to the electrode surface (*5*).

Because of the artificially imposed periodicity of the system, satellite peaks are observed that are equally spaced around the Bragg reflections (Fig. 3) (*19, 28–30*). The absence of higher order satellites may indicate that the interfaces are not as abrupt as the applied square-wave galvanostatic pulses. Following Lashmore and Dariel (*19*), we calculated modulation wavelengths (Λ_x) from Eq. 2, where θ_+ and θ_- are the positions of the high-angle (+) and low-angle (−) satellites, n is the order, and λ is the wavelength of the x-rays (λ = 0.15418 nm):

$$\Lambda_x = \frac{n\,\lambda}{\sin\theta_+ - \sin\theta_-} \quad (2)$$

Table 2 compares the modulation wavelengths calculated from anodic coulombs (Λ_F) and x-ray satellite spacing (Λ_x) for $Tl_aPb_bO_c/Tl_dPb_eO_f$ superlattices deposited at various currents and dwell times. The modulation wavelength was varied systematically from 5.8 to 8.5 nm, and there was excellent agreement between Λ_F and Λ_x. The results in Table 2 also suggest that it is possible to deposit superlattices in this system with a range of compositions [i_b was constant for all five samples, but values of 1.0 mA (Pb/Tl = 2.5) and 5.0 mA (Pb/Tl = 7.3) were used for i_a].

The ability to deposit alternating layers of $Tl_aPb_bO_c$ with a wide range of compositions should prove to be important when fabricating quantum devices based on these materials. The oxides in this system are fascinating because they exhibit the high electrical conductivity of metals with the optical properties of semiconductors. Thallium(III) oxide, for instance, is a degenerate n-type semiconductor with a bandgap of 1.4 eV and a room temperature resistivity of only 70 μohm-cm (*5, 7, 25*). The high conductivity is due to native oxygen vacancies. Lead(IV) oxide is also n-type degenerate but has a larger bandgap of approximately 1.8 eV (*9*). Hence, these materials may function as multiple quantum wells when the modulation wavelength is in the nanometer range. In addition, it will be interesting to compare the electrical properties of these artificially layered materials to those of the layered high-temperature ceramic superconductors that contain thallium and lead (*31*).

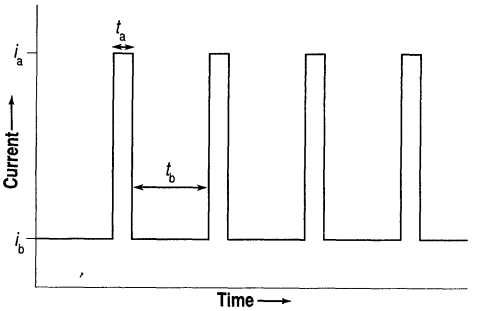

Fig. 2. Generalized double galvanostatic pulse used to electrodeposit superlattices. The layer thickness is proportional to the product of current and time (see Eq. 1).

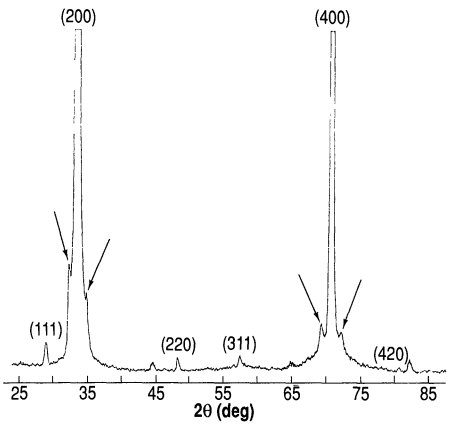

Fig. 3. X-ray diffraction pattern for the $Tl_aPb_bO_c/Tl_dPb_eO_f$ superlattice with a modulation wavelength of 7.3 nm. Note satellites marked by arrows around the (200) and (400) reflections at 2θ values of 34° and 71°. We electrodeposited the material by alternately pulsing at 5 mA for 0.5 s and 0.05 mA for 50 s in a solution of 0.005M $TlNO_3$ and 0.1M $Pb(NO_3)_2$ in 5M NaOH. The shaded peaks are from the 430 stainless steel substrate. The x-ray radiation was CuKα (λ = 0.15418 nm).

REFERENCES AND NOTES

1. C. M. Falco and I. K. Schuller, in *Synthetic Modulated Structures*, L. L. Chang and B. C. Giessen, Eds. (Academic Press, Orlando, FL, 1985), pp. 339–362.
2. C. R. Leavens and R. Taylor, Eds., *Interfaces, Quantum Wells, and Superlattices* (North Atlantic Treaty Organization Series B: Physics, vol. 179) (Plenum, New York, 1988)
3. T. Terashima and Y. Bando, *J. Appl. Phys.* **56**, 3445 (1984).
4. E. E. Mendez and K. von Klitzing, Eds., *Physics and Applications of Quantum Wells and Superlattices* (North Atlantic Treaty Organization Series B: Physics, vol. 170) (Plenum, New York, 1987).

28 August 1989; accepted 27 November 1989

5. R. J. Phillips, M. J. Shane, J. A. Switzer, *J. Mater. Res.* **4**, 923 (1989).
6. J. A. Switzer, *Am. Ceram. Soc. Bull.* **66**, 1521 (1987).
7. ———, *J. Electrochem. Soc.* **133**, 722 (1986).
8. ———, U.S. Patents, 4,492,811; 4,495,046; 4,521,499; 4,592,807; 4,626,322; and 4,608,750.
9. W. Mindt, *J. Electrochem. Soc.* **116**, 1076 (1969).
10. A. C. Ramamurthy and T. Kuwana, *J. Electroanal. Chem.* **135**, 243 (1982).
11. J. C. G. Thanos and D. W. Wabner, *ibid.* **182**, 25 (1985).
12. M. Sakai, T. Sekine, Y. Yamazaki, *J. Electrochem. Soc.* **130**, 1631 (1983).
13. W. Tillmetz and D. W. Wabner, *Z. Naturforsch. Teil B* **39**, 594 (1984).
14. A. Brenner, *Electrodeposition of Alloys* (Academic Press, New York, 1963), vol. 2, p. 589.
15. U. Cohen, F. B. Koch, R. Sard, *J. Electrochem. Soc.* **130**, 1987 (1983).
16. D. Tench and J. White, *Metall. Trans. A* **15**, 2039 (1984).
17. C. Ogden, *Plat. Surf. Finish.* **5**, 133 (1986).
18. J. Yahalom and O. Zadok, *J. Mater. Sci.* **22**, 499 (1987).
19. D. S. Lashmore and M. P. Dariel, *J. Electrochem. Soc.* **135**, 1218 (1988).
20. J. Yahalom *et al.*, *J. Mater. Res.* **4**, 755 (1989).
21. A. R. Despic, V. D. Jovic, S. Spaic, *J. Electrochem. Soc.* **136**, 1651 (1989).
22. T. W. Barbee, F. Spaepen, L. Greer, Eds., *Multilayers: Synthesis, Properties and Non-Electronic Applications* (Materials Research Society Symposium Proceedings 103, Materials Research Society, Pittsburgh, PA, 1988).
23. L. H. Bennett *et al.*, *J. Magn. Magn. Mater.* **67**, 239 (1987).
24. U. Atzmony, L. J. Swartzendruber *et al.*, *ibid.* **69**, 237 (1987).
25. V. N. Shukla and G. P. Wirtz, *J. Am. Ceram. Soc.* **60**, 253 (1977).
26. P. T. Moseley, J. L. Hutchison, M. A. M. Bourke, *J. Electrochem. Soc.* **129**, 876 (1982).
27. Y. Syono and S. Akimoto, *Mater. Res. Bull.* **3**, 153 (1968).
28. H. E. Cook and J. E. Hilliard, *J. Appl. Phys.* **40**, 2191 (1969).
29. A. Segmuller, P. Krishna, L. Esaki, *J. Appl. Crystallogr.* **10**, 1 (1977).
30. I. K. Schuller and C. M. Falco, *Surface Sci.* **113**, 443 (1982).
31. For a review of high-temperature superconductors, see A. W. Sleight, *Science* **242**, 1519 (1988).
32. One of the authors (J.A.S.) thanks Mitsubishi Corporation for financial support through a Mitsubishi Kasei faculty development award. We also thank Unocal Corporation for donation of all of the electrochemical instrumentation used in this research, and we thank G. McManus for assistance with x-ray diffraction and scanning electron microscopy.

28 August 1989; accepted 27 November 1989

Stratospheric Hydroperoxyl Measurements

WESLEY A. TRAUB, DAVID G. JOHNSON, KELLY V. CHANCE

The hydroperoxyl radical (HO_2) plays a key role in stratospheric chemistry through the HO_x catalytic cycle of ozone destruction. Earlier measurements of stratospheric HO_2 have given mixed results; some measured mixing ratios greatly exceed theoretical predictions. Measurements of HO_2 have now been made with a balloon-borne far-infrared spectrometer. The measured daytime profile is in excellent agreement with theory up to 40 kilometers; above this level the measurements exceed theory by 30 percent, perhaps because of underprediction of ozone at these altitudes. The nighttime HO_2 profile is strongly depressed with respect to the daytime profile, in general agreement with theory.

IN THE MIDDLE STRATOSPHERE (*1*), HO_x chemistry is driven by excited atomic oxygen, $O(^1D)$, which is produced by solar ultraviolet (UV) photolysis of ozone (O_3). The $O(^1D)$ reacts with water vapor to create OH, which in turn reacts with O_3 to yield HO_2, the hydroperoxyl radical. Together HO_2 and OH then catalytically destroy O_3 and O. It is believed that HO_x reactions are responsible for ~90% of the total O_3 and O losses at 60 km, but only ~10% at 40 km and below (*2*). The HO_x reactions also provide important production and loss terms in the chemistry of active Cl and N species.

The full atmospheric chemistry of HO_2 is relatively complex and includes at least three production and seven loss reactions, not all of which have well-understood reaction rates (*2, 3*). However, in a simplified picture, the strong attenuation of solar UV with depth in the stratosphere suggests that daytime HO_2 will be relatively more abundant above the ozone layer (~35 km) than below. At night, the concentration of HO_2 plummets because of loss reactions and the absence of UV light; the largest relative change occurs in the lower stratosphere, where loss reactions are most rapid.

Theoretical models of stratospheric chemistry are widely used to predict future response of the ozone layer to both natural and anthropogenic changes. The veracity of these predictions depends upon the accuracy and completeness of the models. Clearly, one way to verify the models is to see if they concur with measurements of the present stratosphere. For the case of HO_2, three types of measurements have been reported: two in situ methods [resonance fluorescence (*4*) and matrix isolation (*5*)] and a ground-based method [millimeter-wave (*6*)]. In a recent assessment (*2*) of theory and observation, the in situ measurements of HO_2 were found to be high with respect to current theory, but the ground-based measurements were in agreement; as a result, if the in situ observations are correct, then substantial changes would be required in our understanding of both HO_x chemistry and the ozone budget.

We have measured HO_2 with a far-infrared spectrometer (FIRS-2) that was mounted on a balloon-borne platform and viewed the atmosphere above the earth's limb through a small telescope (*7, 8*). The FIRS-2 had an effective spectral resolution of 0.008 cm^{-1} over the range 80 to 250 cm^{-1}. This region includes many molecular rotational lines that are thermally populated at stratospheric temperatures (*9*). Because the earth's troposphere is essentially opaque in

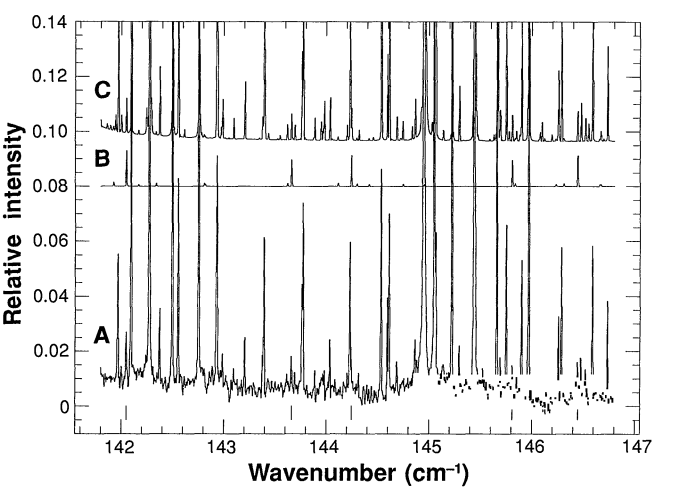

Fig. 1. (**A**) Measured daytime stratospheric spectrum from 142 to 147 cm^{-1} (see text). The intensity is normalized to a 277-K blackbody. (**B**) Theoretical spectrum showing only HO_2, vertically offset by +0.08 for clarity. (**C**) Theoretical spectrum including all species, also offset by +0.08 [the apparent baseline difference between (B) and (C) is caused by an empirically determined continuum component in our model; the physical origin of this continuum is thought to be the far wings of water vapor lines]. Tic marks at bottom show the five HO_2 lines used in our analysis.

Harvard-Smithsonian Center for Astrophysics, 60 Garden Street, Cambridge, MA 02138.